Multiterminal Josephson junctions with tunable topological properties

Panch Ram [1,2,*] Detlef Beckmann [3] Romain Danneau [3] and Wolfgang Belzig [2,†]
[1]*Department of Physics, Indian Institute of Technology (BHU), Varanasi, Uttar Pradesh 221005, India*
[2]*Fachbereich Physik, Universität Konstanz, D-78457 Konstanz, Germany*
[3]*Institute for Quantum Materials and Technologies, Karlsruhe Institute of Technology, Karlsruhe D-76021, Germany*

(Received 24 January 2025; revised 7 October 2025; accepted 19 November 2025; published 8 December 2025)

Since the discovery of the Andreev reflection process at normal-metal/superconductor junctions and the corresponding Andreev bound states in superconductor/normal-metal/superconductor junctions, various multiterminal Josephson junctions have been studied to explore many exotic phases of quantum matter, where the formation of Andreev bound states in the normal region account for dissipationless supercurrent and play a central role in determining exotic properties. Recently, an intriguing aspect of the multiterminal Josephson junctions has been proposed to study the topological properties, wherein the Andreev bound states acquire topological characteristics upon tuning the phase differences of superconducting terminals. In this work, we investigate topologically nontrivial phases in four-terminal Josephson junctions based on square and graphene lattices. Additionally, we apply a gating potential that smoothly drives the Andreev bound states from a topologically nontrivial state to a topologically trivial state. Furthermore, we observe that the gating potential in our setup produces similar physics of the topological Andreev bound states of the double (single) quantum-dot multiterminal Josephson junctions when the gating potential is small (large) compared to the superconducting energy gap.

DOI: 10.1103/2p7b-2hc2

I. INTRODUCTION

Although the underlying concepts of topology in mathematics have been known since the seventeenth century, the successful integration of this idea into condensed matter physics is relatively recent, emerging only about two decades ago with the discovery of novel topological quantum materials, such as topological insulators [1–4], topological semimetals [5], and topological superconductors [6]. The topological insulators exhibit insulating bulk states while supporting conducting surface states at the edges, whereas the electronic states of the topological semimetals demonstrate responses to externally applied electric and magnetic fields. In the case of the topological superconductors, the time-reversal symmetry is broken in two-dimensional planar systems, and they differ fundamentally from the Bose-Einstein condensate of Cooper pairs. Moreover, the study of topological superconductors has advanced the development of Majorana fermions, which are their own antiparticles and obey non-Abelian braiding statistics [7–9]. These Majorana zero-energy modes are particularly significant for their potential use as qubits in topological quantum computation [10–13].

The nontrivial topology in such real-world materials is often hard coded, requiring some specific interactions such as strong spin-orbit coupling. However, a branch of topological investigations has recently gained attention in the condensed matter community—synthetic quantum matters—where internal degrees of freedom can be easily tuned, offering greater control over topological properties. Examples of such synthetic quantum systems include topological photonics [14,15], topological driven Floquet systems [16], topological electrical circuits [17], and multiterminal Josephson junctions (MTJJs) [18–31]. The MTJJs, in particular, comprise multiple BCS-type superconducting leads and can, in principle, host topologically nontrivial Andreev bound states (ABSs) in synthetic space of the superconducting phase differences. These topological ABSs result in an integer-valued first Chern number which is related to a quantized transconductance between two superconducting terminals [18]. Moreover, in the MTJJs, a nontrivial higher-dimensional topology can be easily engineered by simply increasing the number of superconducting leads [18,32].

Recently, various types of MTJJs have been synthesized and subjected to experimental measurements; however, a clear signature of the nontrivial topology in such systems remains elusive, due to experimental challenges in achieving the specific conditions required by the scattering region placed in between the superconducting terminals [33–39]. Alternatively, several proposals involving quantum dots coupled with superconducting terminals have been suggested, but these also require specialized coupling between the superconducting terminals, which presents further feasibility limitations [26–28]. More recently, however, a system consisting of a double quantum dot coupled with four superconducting terminals has been proposed, which may be experimentally feasible [40]. One of the key findings

*Contact author: panchram.phy@itbhu.ac.in
†Contact author: wolfgang.belzig@uni-konstanz.de

in [40] indicates that the realization of topologically nontrivial Andreev bound states (ABSs) requires a system comprising at least two coupled quantum dots within a multiterminal Josephson junction setting. The graphene based MTJJs have also been extensively studied for their transport properties, including Cooper pair quartets [41,42] and supercurrent flow across multiple leads [33]. Recent efforts have focused on probing Andreev bound state (ABS) band structures via local spectroscopy [37]. However, a direct observation of topological ABS spectra remains challenging, as it requires independent control of three superconducting phases. A new study on a four-terminal InAs/Al junction reported signatures of topological ABS bands, though interpretation is limited by the resolution of tunneling spectroscopy [43].

Inspired by the experimental progress toward observing the nontrivial topological ABSs in MTJJs, in this paper, we theoretically investigate the topological properties of Andreev bound states in four-terminal Josephson junctions based on square and graphene lattices. Graphene is ideally suited for experiments on multiterminal Josephson junctions due to the high quality of graphene encapsulated in boron nitride, the gate tunability, and the possibility of forming high-transparency contacts with superconductors [44–56]. Ballistic transport is routinely observed, and the limit of short Josephson junctions can be easily achieved in hybrid structures defined by e-beam lithography. Nonetheless, real-world structures will be much larger than a single quantum dot and incorporate inhomogeneous gate potentials. We therefore focus here on finite-size systems with gate potential included. In the short-junction limit, we demonstrate that the lowest ABSs undergo a topological phase-transition upon tuning the superconducting phase differences between the terminals. In addition, we examine the robustness of these topological ABSs in the presence of an externally applied gate potential in the scattering region. We find that the topological nature of these ABSs remains intact for a large gate potential relative to the superconducting energy gap, before eventually transitioning into a topologically trivial phase.

The rest of the paper is ogranized as follows. In Sec. II, we present the tight-binding model Hamiltonian of MTJJs for both square and graphene lattices, the scattering matrix theory formalism to obtain the ABS energies and the corresponding states, and a numerical method [57] to calculate the Chern number. Section III provides results for the topological phase diagrams, obtained by using the Chern number and minima of the lowest positive ABS energy, in the space of model parameters. Finally, we conclude the paper in Sec. IV.

II. MODEL AND METHOD

A. Hamiltonian

We setup a tight-binding model Hamiltonian for a system of four-terminal Josephson junctions, as shown in Fig. 1, based on square and graphene lattices to study the topologically nontrivial ABSs, $\hat{H} = \hat{H}_0 + \hat{H}_\Delta$. For the square lattice,

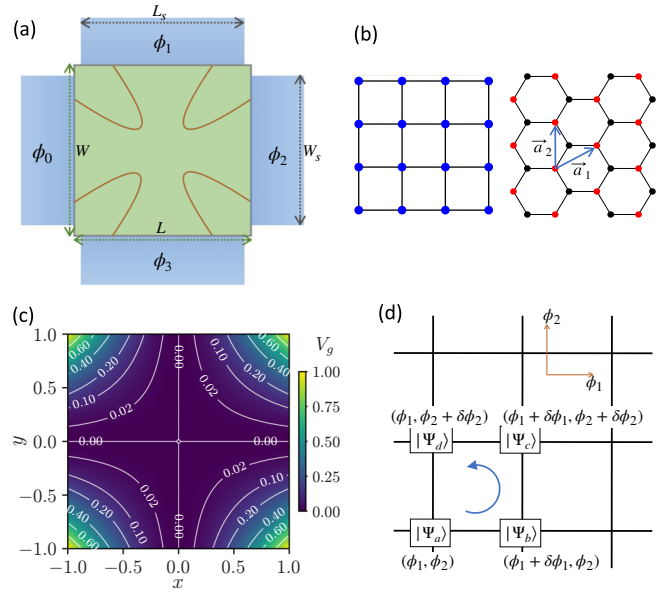

FIG. 1. (a) Schematic illustration of the multiterminal Josephson junctions setup. We consider a system with four superconducting terminals attached with a scattering region, forming Josephson junctions. The scattering region is indicated in light-green with length L and width W whereas the four superconducting (SC) leads are depicted in the light-blue with phases ϕ_α (for $\alpha = 0$ to 3). These semi-infinite horizontal and vertical leads have the corresponding width W_s and length L_s, respectively. Additionally, a schematic of externally applied gating potential, acting only in the scattering region, is shown in orange color, increasing in strength along the diagonals. (b) We setup the system based on square and graphene lattices and employ the KWANT [58] to numerically simulate the tight-binding model Hamiltonians in Eqs. (1) and (2). (c) A typical color plot and contour plot for the applied gating potential of the form $V(x, y) = V_g x^2 y^2$. (d) A discretized mesh grid in (ϕ_1, ϕ_2) space is used to numerically calculate the Chern number, in Eq. (10), by using the Fukui, Hatsugai, and Suzuki method [57].

$$\hat{H}_0 = -t \sum_{\mathbf{r},\boldsymbol{\delta}} \sum_{\sigma} (\hat{c}^\dagger_{\mathbf{r},\sigma} \hat{c}_{\mathbf{r}+\boldsymbol{\delta},\sigma} + \text{H.c.}) + \sum_{\mathbf{r}} \sum_{\sigma} (4t - \mu + V_{\mathbf{r}}) \hat{c}^\dagger_{\mathbf{r},\sigma} \hat{c}_{\mathbf{r},\sigma}, \tag{1a}$$

$$\hat{H}_\Delta = \sum_{\mathbf{r}} (\Delta_{\mathbf{r}} \hat{c}^\dagger_{\mathbf{r},\uparrow} \hat{c}^\dagger_{\mathbf{r},\downarrow} + \Delta^*_{\mathbf{r}} \hat{c}_{\mathbf{r},\downarrow} \hat{c}_{\mathbf{r},\uparrow}), \tag{1b}$$

where the operator $\hat{c}^\dagger_{\mathbf{r},\sigma}(\hat{c}_{\mathbf{r},\sigma})$ creates (annihilates) an electron with spin $\sigma \in \{\uparrow, \downarrow\}$ at lattice site $\mathbf{r} \equiv n_x\hat{x} + n_y\hat{y}$ with $n_x, n_y \in \mathbb{Z}$, and $\boldsymbol{\delta} \equiv \{\pm\hat{x}, \pm\hat{y}\}$ is the nearest-neighbor vector, t and μ are, respectively, the hopping energy amplitude and chemical potential, while $V_{\mathbf{r}} \equiv V(x, y) = V_g x^2 y^2$ is added to account for the gating potential which is only applied in the scattering region. The superconducting pairing $\Delta_{\mathbf{r}} = \Delta e^{i\phi_\alpha}$ is nonzero only for the lattice sites that lie in the superconducting leads, which are labeled for the index $\alpha \in \{0, 1, 2, 3\}$ with the

corresponding phases $\{\phi_\alpha\}$, and accounts for the s-wave singlet superconducting pairing. The onsite energy $4t$ in $\hat{H}_0$ is added to shift the overall energy spectrum.

Similarly, for the graphene lattice,

$$\hat{H}_0 = -t\sum_{\mathbf{r},\boldsymbol{\delta}}\sum_{\sigma}(\hat{a}^\dagger_{\mathbf{r}+\boldsymbol{\delta},\sigma}\hat{b}_{\mathbf{r},\sigma} + \text{H.c.}) + \sum_{\mathbf{r}}\sum_{\sigma}(V_{\mathbf{r}}-\mu)(\hat{a}^\dagger_{\mathbf{r},\sigma}\hat{a}_{\mathbf{r},\sigma} + \hat{b}^\dagger_{\mathbf{r},\sigma}\hat{b}_{\mathbf{r},\sigma}), \quad (2a)$$

$$\hat{H}_\Delta = \sum_{\mathbf{r}}[(\Delta_{\mathbf{r}}\hat{a}^\dagger_{\mathbf{r},\uparrow}\hat{a}^\dagger_{\mathbf{r},\downarrow} + \Delta_{\mathbf{r}+\boldsymbol{\tau}}\hat{b}^\dagger_{\mathbf{r},\uparrow}\hat{b}^\dagger_{\mathbf{r},\downarrow}) + \text{H.c.}], \quad (2b)$$

where $\mathbf{r} \equiv n_1\vec{a}_1 + n_2\vec{a}_2$ is lattice vector with integers $n_1, n_2 \in \mathbb{Z}$, and $\vec{a}_1 = a(\sqrt{3}/2, 1/2)$ and $\vec{a}_2 = a(0,1)$ are the primitive vectors for graphene with lattice constant a. Here, we separately define the creation (annihilation) operators $\hat{a}^\dagger_{\mathbf{r},\sigma}$ and $\hat{b}^\dagger_{\mathbf{r},\sigma}$ ($\hat{a}_{\mathbf{r},\sigma}$ and $\hat{b}_{\mathbf{r},\sigma}$) with spin $\sigma \in \{\uparrow,\downarrow\}$ on two sublattices A and B, respectively, at the lattice site positions $\mathbf{r}$ and $\mathbf{r}+\boldsymbol{\tau}$ with $\boldsymbol{\tau} = a\hat{x}/\sqrt{3}$; see Fig. 1(b). However, we consider the same superconducting pairing $\Delta_{\mathbf{r}} = \Delta_{\mathbf{r}+\boldsymbol{\tau}} \equiv \Delta e^{i\phi_\alpha}$ on both sublattices.

B. Scattering matrix theory approach

To calculate the topological ABSs, we use the KWANT software [58] to set up the tight-binding model Hamiltonians, given in Eqs. (1) and (2) for square and graphene lattices, and employ the scattering matrix theory approach, which is described thoroughly in Ref. [59] for the use of multiterminal Josephson junctions. This approach is well suited for a short-junction limit, i.e., when the length (L) of the scattering region is much smaller than the superconducting coherence length (ξ). In this limit, the ABS energies, $|\varepsilon| < \Delta$, formed due to electron-hole conversion process at all interfaces, are determined by the condition

$$S_A(\varepsilon)S_N(\varepsilon)|\Psi\rangle = |\Psi\rangle, \quad (3)$$

which involves the scattering matrices at the interfaces for Andreev reflection process (S_A) as well as normal reflection process (S_N). Within this approach, their forms can be written as

$$S_A(\varepsilon) = \beta(\varepsilon)\begin{pmatrix}0 & r_A^*\\ r_A & 0\end{pmatrix}, \quad S_N(\varepsilon) = \begin{pmatrix}S(\varepsilon) & 0\\ 0 & S^*(-\varepsilon)\end{pmatrix} \quad (4)$$

with $\beta(\varepsilon) = \sqrt{1-(\varepsilon/\Delta)^2} + i(\varepsilon/\Delta)$ and the Andreev reflection matrix r_A is in diagonal form,

$$r_A = \begin{pmatrix} ie^{i\phi_0}\mathbf{1}_{n_0} & & & \\ & ie^{i\phi_1}\mathbf{1}_{n_1} & & \\ & & ie^{i\phi_2}\mathbf{1}_{n_2} & \\ & & & ie^{i\phi_3}\mathbf{1}_{n_3}\end{pmatrix}, \quad (5)$$

where $\{\mathbf{1}_{n_\alpha}\}$ are the identity matrices for the incoming scattering modes $\{n_\alpha\}$ in the leads $\alpha = 0$ to 3, whereas $S(\varepsilon)(S^*(-\varepsilon))$ corresponds to the electron (hole) scattering matrix block. Utilizing the short-junction limit approximation, i.e., $S(\varepsilon) \approx S(\varepsilon = 0) \equiv s$, we arrive at the following eigenvalue equation for the ABS states:

$$\begin{pmatrix}s^\dagger & 0\\ 0 & s^T\end{pmatrix}\begin{pmatrix}0 & r_A^*\\ r_A & 0\end{pmatrix}|\Psi\rangle = \beta(\varepsilon)|\Psi\rangle. \quad (6)$$

Now, solving Eq. (6) yields the ABS energies and the corresponding eigenstates.

C. Chern number

In our four-terminal Josephson junctions setup, the ABS energies and eigenstates $(\varepsilon_n, |n\rangle$ for the index $n = \pm1, \pm2, \cdots)$ depend on the four superconducting phases. Since out of the four phases only three are independent, we use a gauge variance to fix one phase $\phi_0 = 0$ and determine the ABS energies $|\varepsilon_n| < \Delta$ and wavefunctions with respect to the remaining phases ϕ_α (for $\alpha = 1, 2, 3$) [26,27]. These phases $(\phi_1, \phi_2, \phi_3) \in [0, 2\pi)^3$ form a three-dimensional periodic compact space analogous to the quasimomenta in periodic crystals. In our setup, the lowest positive ABS energies, ε_n for $n = \pm1$, close and open the gap at zero energy upon tuning the phase differences. These phases act as the quasi-momenta in this synthetic dimensions for the topological Andreev bound states. Therefore, for a given phase difference, such as ϕ_3, we define the nth state Chern number in the space of other two phase differences (ϕ_1, ϕ_2) as

$$C_{12}^{(n)} = \frac{1}{2\pi}\int_0^{2\pi}\int_0^{2\pi} B_{12}^{(n)} d\phi_1 d\phi_2, \quad (7)$$

where $B_{12}^{(n)} = \partial_1 A_2^{(n)} - \partial_2 A_1^{(n)}$ is the Berry curvature for the nth state, while $A_{1/2}^{(n)} = i\langle n|\partial_{1/2}|n\rangle$ is the corresponding Berry connection. The $C_{12}^{(n)}$ is quantized to integer values. Similar to the conventional two-dimensional electronic systems where a nonzero Chern number manifest as a quantized Hall conductance [60], the nonzero integer values of $C_{12}^{(n)}$ can be experimentally probed in the topological regime via a transconductance measurement $G_{12} = (-4e^2/h)C_{12}^{\text{GS}}$ between the superconducting leads 1 and 2 [18]. Here h is the Planck constant and e is the elementary charge, and C_{12}^{GS} is the ground-state Chern number at zero temperature which is obtained by summing over all negative-energy eigenstates, i.e., $C_{12}^{\text{GS}} = \sum_n C_{12}^{(n)}$ such that $\varepsilon_n < 0$.

As we only obtain numerical data for the eigenspectrum of Eq. (6), within the KWANT simulation, we use the numerical method developed by Fukui, Hatsugai, and Suzuki in Ref. [57] to calculate the Chern number. Specifically, we discretize the phases $0 < \phi_{1/2} < 2\pi$ into $M \times M$ grid points, with finite difference $\delta\phi_{1/2} = 2\pi/M$, and define the link quantity $U_{\delta\vec{\phi}}^{(n)}(\vec{\phi}) = \langle n(\vec{\phi})|n(\vec{\phi}+\delta\vec{\phi})\rangle$. Here, $\vec{\phi}$ is a grid point vector in the (ϕ_1, ϕ_2) space, and $\delta\vec{\phi}$ represents the step to the next grid point. Then, analogous Berry curvature is evaluated in terms of link quantities as

$$\tilde{B}_{12}^{(n)}(\vec{\phi}) = \ln\big[U_{\delta\phi_1}^{(n)}(\vec{\phi})U_{\delta\phi_2}^{(n)}(\vec{\phi}+\delta\phi_1) \times U_{\delta\phi_1}^{(n)^{-1}}(\vec{\phi}+\delta\phi_2)U_{\delta\phi_2}^{(n)^{-1}}(\vec{\phi})\big]. \quad (8)$$

To better understand these link quantities, we consider the nth eigenstates $|\Psi_a\rangle$, $|\Psi_b\rangle$, $|\Psi_c\rangle$, and $|\Psi_d\rangle$ for a plaquette [see in Fig. 1(d)] at the grid points (ϕ_1, ϕ_2), $(\phi_1+\delta\phi_1, \phi_2)$, $(\phi_1+\delta\phi_1, \phi_2+\delta\phi_2)$, and $(\phi_1, \phi_2+\delta\phi_2)$, respectively. Then the analogous Berry curvature in Eq. (8) is expressed as

$$\tilde{B}_{12}^{(n)}(\vec{\phi}) = \ln[\langle\Psi_a|\Psi_b\rangle\langle\Psi_b|\Psi_c\rangle\langle\Psi_c|\Psi_d\rangle\langle\Psi_d|\Psi_a\rangle]. \quad (9)$$

Finally, the Chern number is obtained by summing over all $M \times M$ grid points as

$$C_{12}^{(n)} = \frac{1}{2\pi} \sum_{\{\vec{\phi}\}} \Im\big[\tilde{B}_{12}^{(n)}(\vec{\phi})\big], \tag{10}$$

where the symbol $\Im$ denotes the imaginary part. Note that $\tilde{B}_{12}^{(n)}$ and $B_{12}^{(n)}$ in Eqs. (8) and (7) are closely related, with $\tilde{B}_{12}^{(n)}(\vec{\phi}) \simeq B_{12}^{(n)}(\vec{\phi})\delta\phi_1\delta\phi_2$.

In the next section, we present the results for the topological phase diagrams of the Chern number C_{12}^{GS} and the $\delta_{\min} \equiv \min_{(\phi_1,\phi_2)}\varepsilon_1$ of lowest Andreev band for both square and graphene lattices. Additionally, we show the evolution of ABS energies ε_n and Berry curvature $B_{12}^{(n)}$ with respect to (ϕ_1, ϕ_2) for different values of ϕ_3. These quantities are calculated using Eqs. (6), (8), and (10). For the calculation, we set $t = 1$, with all energy parameters expressed in units of t, and fix the superconducting pairing value to $\Delta = 0.005t$. A typical value in a conventional superconductor is $\Delta \approx 1.2\,\mathrm{meV}$. For graphene lattice, the hopping energy is approximately $t \approx 2.8\,\mathrm{eV}$ and the lattice constant is $a \approx 0.246\,\mathrm{nm}$, therefore, comparatively $\Delta = 1.2\,\mathrm{meV} \sim 0.43 \times 10^{-3}t$ which leads to the coherence length $\xi = \hbar v_F/\Delta = \sqrt{3}ta/(2\Delta) \approx 2060a = 0.51\mu\mathrm{m}$. Hence, the actual device made of graphene superconducting leads will require size $L_s > \xi(\sim 2060a)$. This is ensured in our calculation by taking the semi-infinite leads in the scattering approach. However, as we consider $\Delta = 0.005t$ (approximately ten times higher than the actual value) in the KWANT calculation, it reduces the superconducting coherence length to $\xi \approx 173a \approx 43\,\mathrm{nm}$ and, consequently, the system size of the scattering region is reduced, allowing for a smaller scattering region and thereby enabling real-time simulations of the topological ABS energy spectra. We consider the scattering region of size $L = 20a \approx 5\,\mathrm{nm}$ and $W = 12a \approx 3\,\mathrm{nm}$. Therefore, $L \approx 0.12\xi$, the system is well within the short junction limit, i.e., $\xi \gg L$.

III. RESULTS

A. Square

For the square lattice, we consider the system size of our four-terminal junctions shown in Figs. 1(a) and 1(b), with the scattering region $L = W = 24a$, whereas the widths of semi-infinite leads 0 and 2 have $W_s = L - 2$, and the lengths of leads 1 and 3 have $L_s = W_s$. We parametrize the global chemical potential as $\mu = (1-\eta)E_1 + \eta E_2$, where $\eta \in (0, 1)$ is an independent parameter. The values of E_1 and E_2 are fixed using the dispersion relation formula for a square lattice, $E_n(k) = 4t - 2t\cos(ka) - 2t\cos(\frac{\pi a}{W_s}n)$, of an ideal semi-infinite sheet of width W_s. We choose the two lowest mode energies $E_1 \equiv E_{n=1}(k=0) \approx 4.07\Delta$ and $E_2 \equiv E_{n=2}(k=0) \approx 16.2\Delta$, and set $E_1 < \mu < E_2$ for $\eta \in (0, 1)$. This condition ensures that only one conducting channel is available in each lead for the Andreev process of electron-hole conversion.

We first set the gating potential to zero (i.e., $V_g = 0$) and present results for the nontrivial topological phases in terms of the ground state Chern number, C_{12}^{GS}, calculated from Eq. (10), and also the corresponding phase boundaries are obtained by evaluating the minimum of the lowest ABS energy $\delta_{\min} \equiv \min_{(\phi_1,\phi_2)}\varepsilon_1$, from Eq. (6), in the parameter space of ϕ_3 and η. Figure 2(a)(i) shows the phase diagram for the Chern number, highlighting large stable regions (yellow and dark purple) where $C_{12}^{\mathrm{GS}} \neq 0$, indicating topologically nontrivial phases, while the gray region, where $C_{12}^{\mathrm{GS}} = 0$, corresponds to a topologically trivial phase. We observe a phase transition from the topologically trivial phase to the nontrivial phase along both the ϕ_3 and η directions. We obtain results similar to the double quantum-dot system attached to four superconducting leads when varing ϕ_3 [40], showing a nontrivial topological phase transition from $C_{12}^{\mathrm{GS}} = 1(-1)$ to $C_{12}^{\mathrm{GS}} = -1(1)$, depending on η, at $\phi_3 = \pi$. Interestingly, by varying η, i.e., the global chemical potential μ, the nontrivial Chern number also changes around $\eta \approx 0.4$ even though the conducting channel for the Andreev process remains fixed. Additionally, we determine the phase boundaries by simply tracking the minimum value of the lowest positive ABS energy, see in Fig. 2(a)(iii). It clearly marks the boundaries where the gap becomes zero, i.e., $\delta_{\min} = 0$. Several plots of C_{12}^{GS} and $\delta_{\min}$ are explicitly shown in Figs. 2(a)(ii) and 2(a)(iv) as a function of ϕ_3 for selected values of $\eta = 0.22, 0.37, 0.68$, and 0.84. Clearly, as η increases, the topologically nontrivial phases for C_{12}^{GS} initially shrink, but after $\eta \approx 0.4$, these regions expand again. However, with further increase in η, the system eventually enters the topologically trivial phase; see also Fig. 2(a)(i).

To better understand these phases, we plot the subgap Andreev energy bands ($\varepsilon_{\pm 1}$) as functions of ϕ_1 and ϕ_2, in Fig. 2(b), at $\eta = 0.22$ for various values of ϕ_3 [shown also in Fig. 2(a)(ii) as inverted triangles]. We observe that the overall Andreev spectrum remains gapped at $\phi_3 = 0$. However, as ϕ_3 increases, both bands touch at zero energy and become gapless at a certain critical value of $\phi_3 \approx 0.21\pi$ at a single point (Weyl point). Further tuning of ϕ_3 leads to reopening of the gap and the system goes into a topologically nontrivial regime with $C_{12}^{\mathrm{GS}} = 1$; see the subplots for $\phi_3 = 0.3\pi$ and 0.6π. The gap closes again at $\phi_3 = \pi$, now at two Weyl points, and opens with increasing $\phi_3 > \pi$, exhibiting another topological phase transition with $C_{12}^{\mathrm{GS}} = -1$ (the Andreev bands for $\pi < \phi_3 \leqslant 2\pi$ are not plotted for brevity, as they look similar to the plots for $0 \leqslant \phi_3 \leqslant \pi$). In Fig. 2(c), we present the Berry curvature B_{12} for the lower Andreev band $\varepsilon_{n=-1}$ at $\eta = 0.22$ for a set of selected values of $\phi_3 = 0, 0.15\pi, 0.25\pi, 0.95\pi, 1.05\pi$. It is evident that B_{12} changes sign at the Weyl point(s) near the critical values of ϕ_3 where the phase transition occurs, for instance, see the second and third subplots of B_{12} near the $\phi_3 = 0.21\pi$ and the last two subplots near $\phi_3 = \pi$ in Fig. 2(c). This demonstrates that the Andreev states exhibit a topologically nontrivial nature in the parameter space of the superconducting phase differences and chemical potential.

Next, we introduce the gating potential (i.e., $V_g \neq 0$) and investigate its effect on the topologically nontrivial phases while keeping the global chemical potential fixed at $\eta = 0.3$ and 0.6, respectively. Both points (blue star markers) are indicated in Fig. 2(a)(i). In Fig. 3, we show the results for C_{12}^{GS} and $\delta_{\min}$ in the parameter space of ϕ_3 and V_g. For $\eta = 0.3$, the stable topologically nontrivial regions expand with increasing strength of V_g, and the Chern number becomes $C_{12}^{\mathrm{GS}} = \pm 1$ for almost the entire range of ϕ_3, before eventually transitioning into the topologically trivial phase with

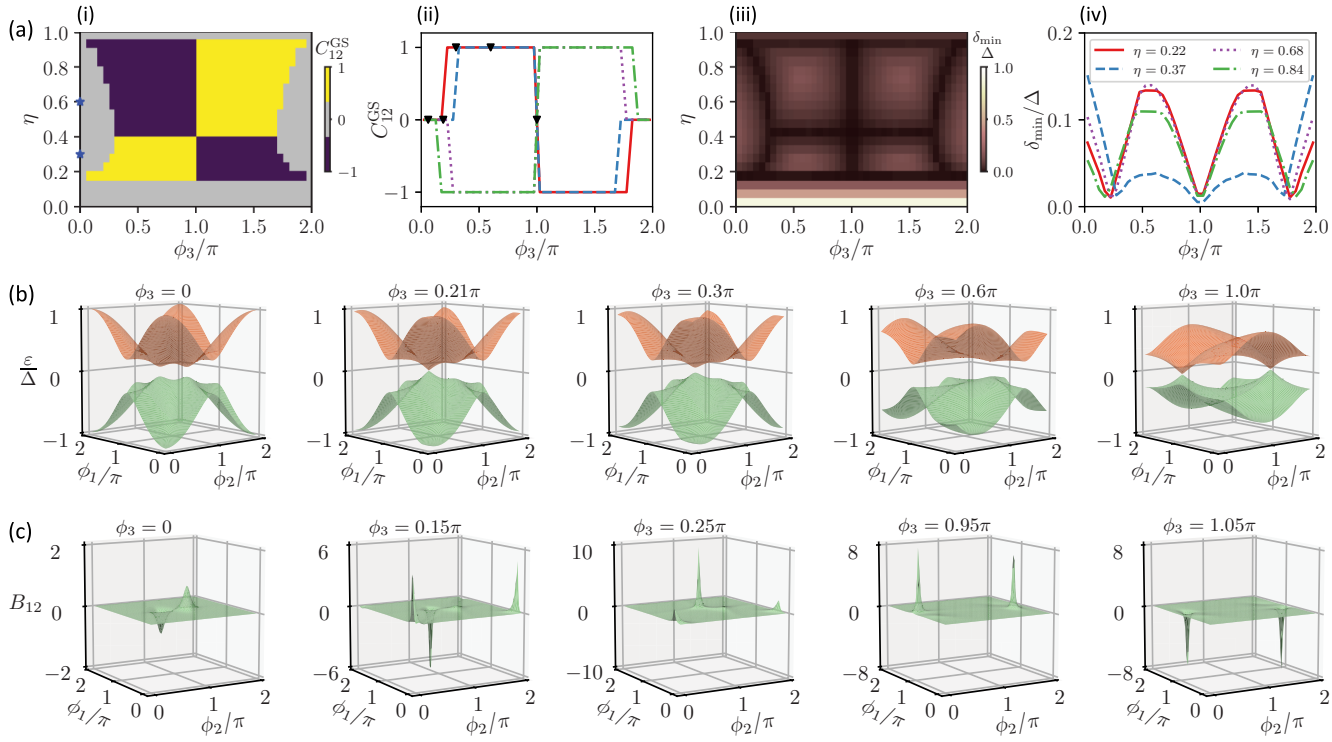

FIG. 2. (a) Topological phase diagram for the Chern number C_{12}^{GS} in (i) and the corresponding phase boundaries from minimum gap δ_{min} (of the lowest ABS energy) in (iii) are plotted in the parameters space (ϕ_3, η) when the gating potential is set to zero, i.e., $V_g = 0$, whereas, they are also shown for a few selected values of η in (ii) and (iv). (b), (c) At a fixed $\eta = 0.22$, the Andreev-energy dispersions $\varepsilon_{\pm 1}$ (in unit of Δ) and the Berry curvature B_{12} (for the lower band) with respect to the phase differences ϕ_1 and ϕ_2 for a set of different ϕ_3 values. The chosen ϕ_3 values are shown in the corresponding plots of (b) and (c); while particularly for the $\varepsilon_{\pm 1}$, they are also shown in (a)(ii) as inverted black triangles.

$C_{12}^{GS} = 0$, see in Fig. 3(a). These phase transition boundaries are again accurately captured by the condition $\delta_{min} = 0$, as shown in Fig. 3(b). Interestingly, for $\eta = 0.6$ in Fig. 3(c), we observe that tuning V_g, the nontrivial phase transition changes from $C_{12}^{GS} = -1(1)$ to $C_{12}^{GS} = 1(-1)$ well before the system transitions into the trivial phase. The minima of the Andreev lower band again show these phase boundaries; see Fig. 3(d).

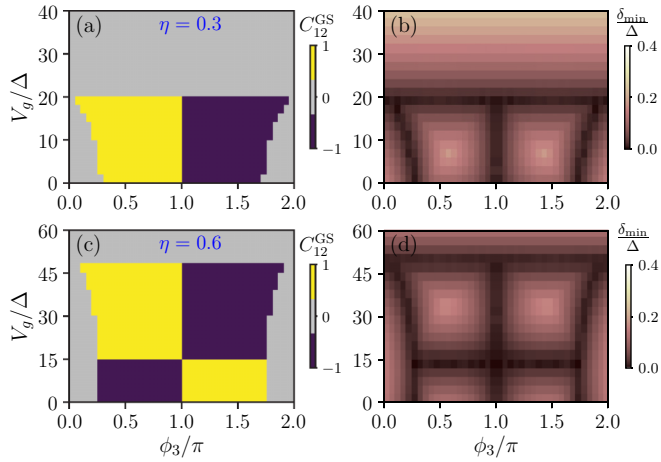

FIG. 3. Topological phases for Chern number C_{12}^{GS} and the corresponding phase boundaries from δ_{min} with respect to ϕ_3 and V_g for fixed values of $\eta = 0.3$ and 0.6.

Overall, we find that the topologically nontrivial phases remain robust even when the gating potential is turned on. Remarkably, V_g enhances the stable regions of topologically nontrivial phases for moderate to large values compared to the superconducting energy gap.

B. Graphene

For the graphene lattice, we set up the four-terminal system as shown in Figs. 1(a) and 1(c). The system size for the scattering region is $L = 20a$ and $W = 12a$; however, $W_s = W$ for the leads 0 and 2, while $L_s = W_s$ for the leads 1 and 3, respectively. Similar to the square lattice, we parametrize the global chemical potential as $\mu = (1-\eta)E_1 + \eta E_2$, where E_1 and E_2 are fixed using the conduction band dispersion relation: $E_n(k) = t\sqrt{1 + 4\cos(\frac{ka}{2})\cos(\frac{\pi a}{W_s}n) + \cos^2(\frac{\pi a}{W_s}n)}$ for an ideal semi-infinite sheet of armchair graphene with width W_s. We fix $E_1 < \mu < E_2$ for $\eta \in (0, 1)$ by choosing the two lowest energy modes $E_1 \equiv E_{n=4W_s/3}(k = 0) = 0$ and $E_2 \equiv E_{n=4W_s/3+1}(k = 0) \approx 21.7\Delta$, respectively.

Now, we present the results for the topological phase diagram of the graphene based four-terminal system. In Figs. 4(a) and 4(b), we plot C_{12}^{GS} and δ_{min}, respectively, in the parameter space (ϕ_3, η) for $V_g = 0$. Notice that initially the system remains in the topologically trivial phase with $C_{12}^{GS} = 0$ as η is tuned. However, it transitions into the topologically nontrivial phases with $C_{12}^{GS} = \pm 1$ upon further tuning. Eventually, it reenters the trivial phase as η approaches 1. Additionally, unlike

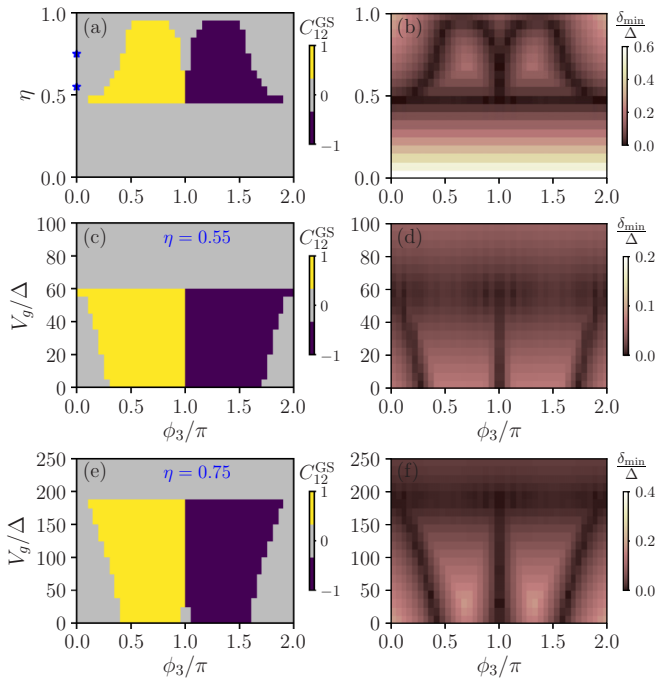

FIG. 4. (a), (b) Topological nontrivial phases for the graphene lattice, obtained from the Chern number C_{12}^{GS} and corresponding phase boundaries from δ_{min}, in parameters space of ϕ_3 and η when the gating potential is absent $V_g = 0$. For fixed $\eta = 0.55$ in (c), (d) and $\eta = 0.75$ in (e), (f), the topologically nontrivial phases are robust and evolve upon tuning V_g.

the square lattice, we observe a bifurcation around the phase transition point $\phi_3 = \pi$ of the topologically nontrivial phases. These phase boundaries are also clearly observed in Fig. 4(b) where δ_{min} becomes zero. Next, we show the results in the presence of V_g for fixed η in the parameter space (ϕ_3, V_g). For $\eta = 0.55$ in Figs. 4(c) and 4(d) we observe a phase diagram similar to that in Figs. 3(a) and 3(b) for the square lattice. Furthermore, when we set $\eta = 0.75$, the bifurcation around $\phi_3 = \pi$ closes as V_g increases. In Figs. 4(e) and 4(f), we notably do not observe the phase transition between the topologically nontrivial phases upon tuning V_g, unlike the case in the square lattice in Figs. 3(c) and 3(d). Nevertheless, it is present along ϕ_3, which is the common feature of both lattices.

C. Bogoliubov-de Gennes method

In this section, we validate the results obtained from the scattering matrix theory approach in the previous two sections using the Bogoliubov-de Gennes (BdG) method. Unlike the scattering matrix approach, where the electron and hole normal-state S-matrices $S(\varepsilon)$ and $S^*(-\varepsilon)$ are approximated as $S(\varepsilon) \approx S(\varepsilon = 0)$, which is only valid in the short-junction limit, the BdG method is numerically exact and does not impose such a constraint and is applicable across all junction regimes. However, the BdG method involves diagonalizing the full Hamiltonian matrix, which restricts its applicability to relatively small system sizes. Nevertheless, the system size considered here, determined by the superconducting coherence length ξ for $\Delta = 0.005t$, remains numerically feasible using sparse matrix techniques.

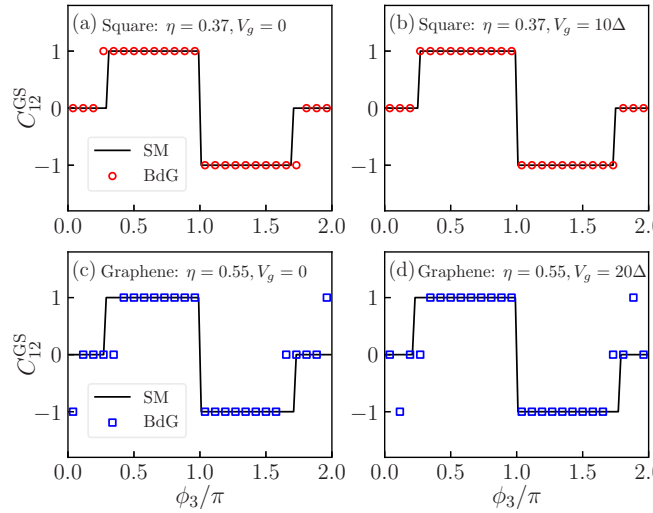

FIG. 5. Chern number C_{12}^{GS} vs ϕ_3 obtained from the scattering matrix (SM) method (solid line) and the BdG method (markers) for both the lattices in the absence and presence of gating potential V_g.

We now consider a system with the superconducting leads of finite length attached to the scattering region, as shown in Fig. 1(a), and set up the Bogoliubov-de Gennes Hamiltonian,

$$H_{BdG} = \begin{pmatrix} H_0 & \Delta_{\mathbf{r}} \\ \Delta_{\mathbf{r}}^* & -H_0 \end{pmatrix}, \tag{11}$$

for both the lattices in the KWANT [58]. The Hamiltonain H_{BdG} is written in the particle-hole basis using the model Hamiltonians given in Eqs. (1) and (2) for square and graphene lattices. We numerically compute the full energy spectrum by diagonalizing the H_{BdG} Hamiltonian matrix in Eq. (11) and sort the Andreev subgap energy states with $|\varepsilon| < \Delta$ to calculate the topological Chern number. The length of the SC leads is set to $L_s \simeq 12L$ to ensure the short junction limit for $\Delta = 0.005t$. We use a standard sparse matrix technique to numerically diagonalize the large H_{BdG} matrix. The system size and model parameters are considered the same as those used in Secs. III A and III B for the scattering matrix (SM) method for square and graphene lattices. In Fig. 5 we show the plots of the topological Chern number C_{12}^{GS} with respect to ϕ_3, which are obtained using the BdG method (markers) and are compared with the SM method (solid line) when V_g is absent and present at a specific value of $\eta = 0.37$ (square) and 0.55 (graphene). Clearly, in Figs. 5(a) and 5(b), both methods provide remarkable agreement, except that the BdG method shows a slightly broader range for the topologically nontrivial phase with $C_{12}^{GS} = \pm 1$ when gating potential is absent ($V_g = 0$); see in Fig. 5(a). For the graphene lattice, shown in Figs. 5(c) and 5(d), we observe that the BdG method shows the phase transition between the topologically trivial to nontrivial phases. However, the BdG data do not exactly fall on the SM line. Nonetheless, the values of the Chern number remain $C_{12}^{GS} = \pm 1$ or $C_{12}^{GS} = 0$ throughout. Overall, we find that the Andreev states calculated using both methods exhibit topological phase transitions in our multiterminal Josephson junctions setup for the square and graphene lattices.

IV. CONCLUSION

We have investigated the topologically nontrivial phases, arising due to the Andreev bound states, in the multiterminal Josephson junctions based on square and graphene lattices. By setting the tight-binding models system in the KWANT software [58] and employing the scattering matrix theory and the Bogoliubov-de Gennes theory in the short-junction limit, we have studied the topological nature of the Andreev bound states both in the absence and presence of an externally applied gating potential in the scattering region of MTJJs. Without the gating potential, i.e., when $V_g = 0$, we find that the topologically nontrivial stable phases exist with $C_{12}^{\mathrm{GS}} = \pm 1$ in a larger region of the parameter space defnined by the superconducting phase difference ϕ_3 and the global chemical potential μ. The phase transitions are marked by closing and opening of the Andreev energy bands with respect to the superconducting phase differences for suitable model parameter values. Interestingly, we also observe phase transitions between the topologically nontrivial phases upon tuning ϕ_3 and μ for the square lattice, however, this feature is only present along ϕ_3 in the case of graphene, as shown in Figs. 2(a) and 4(a). Moreover, these nontrivial topological phases are present even when the gating potential V_g is introduced, remaining stable for moderate to large values of V_g relative to Δ. However, the system enters a topologically trivial phase of ABSs, with $C_{12}^{\mathrm{GS}} = 0$, upon further increase of V_g. Hence, the gating potential V_g produces physics similar to that of topological ABSs in a double (single) quantum dot coupled to four Josephson junctions [40]. Additionally, for a fixed μ, we observe that phase transitions also occur between the topologically nontrivial phases in response to V_g for the square lattice, whereas this feature is absent along the V_g for the graphene. Our results demonstrate that the topological properties can persist in experimentally relevant finite-size systems with gate potentials included.

ACKNOWLEDGMENTS

This work was funded by the Deutsche Forschungsgemeinschaft (DFG, German Research Foundation) Grant No. 467596333. This work was partly supported by the Helmholtz Association through program NACIP. P.R. also acknowledges IIT (BHU) for providing computational facilities.

DATA AVAILABILITY

The data that support the findings of this article are openly available [61].

[1] K. v. Klitzing, G. Dorda, and M. Pepper, New method for high-accuracy determination of the fine-structure constant based on quantized Hall resistance, Phys. Rev. Lett. **45**, 494 (1980).
[2] Y. Hatsugai, Chern number and edge states in the integer quantum Hall effect, Phys. Rev. Lett. **71**, 3697 (1993).
[3] C. L. Kane and E. J. Mele, Z_2 Topological order and the quantum spin Hall effect, Phys. Rev. Lett. **95**, 146802 (2005).
[4] M. Z. Hasan and C. L. Kane, *Colloquium*: Topological insulators, Rev. Mod. Phys. **82**, 3045 (2010).
[5] N. P. Armitage, E. J. Mele, and Ashvin Vishwanath, Weyl and Dirac semimetals in three-dimensional solids, Rev. Mod. Phys. **90**, 015001 (2018).
[6] M. Sato and Y. Ando, Topological superconductors: A review, Rep. Prog. Phys. **80**, 076501 (2017).
[7] Jason Alicea, New directions in the pursuit of Majorana fermions in solid state systems, Rep. Prog. Phys. **75**, 076501 (2012).
[8] C. W. J. Beenakker, Search for Majorana fermions in superconductors, Annu. Rev. Condens. Matter Phys. **4**, 113 (2013).
[9] M. Sato and S. Fujimoto, Majorana fermions and topology in superconductors, J. Phys. Soc. Jpn. **85**, 072001 (2016),.
[10] S. Das Sarma, M. Freedman, and C. Nayak, Majorana zero modes and topological quantum computation, npj Quantum Inf. **1**, 15001 (2015).
[11] M. T. Deng, S. Vaitiekėnas, E. B. Hansen, J. Danon, M. Leijnse, K. Flensberg, J. Nygård, P. Krogstrup, and C. M. Marcus, Majorana bound state in a coupled quantum-dot hybrid-nanowire system, Science **354**, 1557 (2016),.
[12] D. Aasen, M. Hell, R. V. Mishmash, A. Higginbotham, J. Danon, M. Leijnse, T. S. Jespersen, J. A. Folk, C. M. Marcus, K. Flensberg, and J. Alicea, Milestones toward Majorana-based quantum computing, Phys. Rev. X **6**, 031016 (2016).
[13] T. Karzig, C. Knapp, R. M. Lutchyn, P. Bonderson, M. B. Hastings, C. Nayak, J. Alicea, K. Flensberg, S. Plugge, Y. Oreg, C. M. Marcus, and M. H. Freedman, Scalable designs for quasiparticle-poisoning-protected topological quantum computation with Majorana zero modes, Phys. Rev. B **95**, 235305 (2017).
[14] L. Lu, J. D. Joannopoulos, and M. Soljačić, Topological photonics, Nat. Photon. **8**, 821 (2014).
[15] T. Ozawa, H. M. Price, A. Amo, N. Goldman, M. Hafezi, L. Lu, M. C. Rechtsman, D. Schuster, J. Simon, O. Zilberberg, and I. Carusotto, Topological photonics, Rev. Mod. Phys. **91**, 015006 (2019).
[16] M. S. Rudner and N. H. Lindner, Band structure engineering and non-equilibrium dynamics in floquet topological insulators, Nat. Rev. Phys. **2**, 229 (2020).
[17] S. Imhof, C. Berger, F. Bayer, J. Brehm, L. W. Molenkamp, T. Kiessling, F. Schindler, C. H. Lee, M. Greiter, T. Neupert, and R. Thomale, Topolectrical-circuit realization of topological corner modes, Nat. Phys. **14**, 925 (2018).
[18] R.-P. Riwar, M. Houzet, J. S. Meyer, and Y. V. Nazarov, Multi-terminal Josephson junctions as topological matter, Nat. Commun. **7**, 11167 (2016).
[19] E. Eriksson, R.-P. Riwar, M. Houzet, J. S. Meyer, and Y. V. Nazarov, Topological transconductance quantization in a four-terminal Josephson junction, Phys. Rev. B **95**, 075417 (2017).
[20] H.-Y. Xie, M. G. Vavilov, and A. Levchenko, Topological Andreev bands in three-terminal Josephson junctions, Phys. Rev. B **96**, 161406 (2017).

[21] H.-Y. Xie, M. G. Vavilov, and A. Levchenko, Weyl nodes in Andreev spectra of multiterminal Josephson junctions: Chern numbers, conductances, and supercurrents, Phys. Rev. B **97**, 035443 (2018).

[22] O. Deb, K. Sengupta, and D. Sen, Josephson junctions of multiple superconducting wires, Phys. Rev. B **97**, 174518 (2018).

[23] H.-Y. Xie and A. Levchenko, Topological supercurrents interaction and fluctuations in the multiterminal Josephson effect, Phys. Rev. B **99**, 094519 (2019).

[24] L. P. Gavensky, G. Usaj, and C. A. Balseiro, Topological phase diagram of a three-terminal Josephson junction: From the conventional to the Majorana regime, Phys. Rev. B **100**, 014514 (2019).

[25] M. Houzet and J. S. Meyer, Majorana-Weyl crossings in topological multiterminal junctions, Phys. Rev. B **100**, 014521 (2019).

[26] R. L. Klees, G. Rastelli, J. C. Cuevas, and W. Belzig, Microwave spectroscopy reveals the quantum geometric tensor of topological Josephson matter, Phys. Rev. Lett. **124**, 197002 (2020).

[27] R. L. Klees, J. C. Cuevas, W. Belzig, and G. Rastelli, Ground-state quantum geometry in superconductor–quantum dot chains, Phys. Rev. B **103**, 014516 (2021).

[28] I. Septembre, J. S. Meyer, D. D. Solnyshkov, and G. Malpuech, Weyl singularities in polaritonic multiterminal Josephson junctions, Phys. Rev. B **107**, 165301 (2023).

[29] L. P. Gavensky, G. Usaj, and C. A. Balseiro, Multi-terminal Josephson junctions: A road to topological flux networks, Europhys. Lett. **141**, 36001 (2023).

[30] R.-P. Riwar, Fractional charges in conventional sequential electron tunneling, Phys. Rev. B **100**, 245416 (2019).

[31] M. A. Javed, J. Schwibbert, and R.-P. Riwar, Fractional Josephson effect versus fractional charge in superconducting–normal metal hybrid circuits, Phys. Rev. B **107**, 035408 (2023).

[32] H. Weisbrich, R. L. Klees, G. Rastelli, and W. Belzig, Second Chern number and non-Abelian Berry phase in topological superconducting systems, PRX Quantum **2**, 010310 (2021).

[33] A. W. Draelos, M.-T. Wei, A. Seredinski, H. Li, Y. Mehta, K. Watanabe, T. Taniguchi, I. V. Borzenets, F. Amet, and G. Finkelstein, Supercurrent flow in multiterminal graphene Josephson junctions, Nano Lett. **19**, 1039 (2019).

[34] N. Pankratova, H. Lee, R. Kuzmin, K. Wickramasinghe, W. Mayer, J. Yuan, M. G. Vavilov, J. Shabani, and V. E. Manucharyan, Multiterminal Josephson effect, Phys. Rev. X **10**, 031051 (2020).

[35] E. G. Arnault, T. F. Q. Larson, A. Seredinski, L. Zhao, S. Idris, A. McConnell, K. Watanabe, T. Taniguchi, I. Borzenets, F. Amet, and G. Finkelstein, Multiterminal inverse AC Josephson effect, Nano Lett. **21**, 9668 (2021).

[36] V. Chandrasekhar, Probing the topological band structure of diffusive multiterminal Josephson junction devices with conductance measurements, Appl. Phys. Lett. **121**, 222601 (2022).

[37] M. Coraiola, D. Z. Haxell, D. Sabonis, H. Weisbrich, A. E. Svetogorov, M. Hinderling, S. C. ten Kate, E. Cheah, F. Krizek, R. Schott, W. Wegscheider, J. C. Cuevas, W. Belzig, and F. Nichele, Phase-engineering the Andreev band structure of a three-terminal Josephson junction, Nat. Commun. **14**, 6784 (2023).

[38] C. G. Prosko, W. D. Huisman, I. Kulesh, D. Xiao, C. Thomas, M. J. Manfra, and S. Goswami, Flux-tunable Josephson effect in a four-terminal junction, Phys. Rev. B **110**, 064518 (2024).

[39] M. Wisne, Y. Deng, I. M. A. Lilja, P. J. Hakonen, and V. Chandrasekhar, Mapping the topological proximity-induced gap in multiterminal Josephson junctions, Phys. Rev. Lett. **133**, 246601 (2024).

[40] L. Teshler, H. Weisbrich, J. Sturm, R. L. Klees, G. Rastelli, and W. Belzig, Ground state topology of a four-terminal superconducting double quantum dot, SciPost Phys. **15**, 214 (2023).

[41] A. Freyn, B. Doucot, D. Feinberg, and R. Melin, Production of nonlocal quartets and phase-sensitive entanglement in a superconducting beam splitter, Phys. Rev. Lett. **106**, 257005 (2011).

[42] K.-F. Huang, Y. Ronen, R. Mélin, D. Feinberg, K. Watanabe, T. Taniguchi, and P. Kim, Evidence for 4e charge of cooper quartets in a biased multi-terminal graphene-based Josephson junction, Nat. Commun. **13**, 3032 (2022).

[43] T. Antonelli, M. Coraiola, D. C. Ohnmacht, A. E. Svetogorov, D. Sabonis, S. C. ten Kate, E. Cheah, F. Krizek, R. Schott, J. C. Cuevas, W. Belzig, W. Wegscheider, and F. Nichele, Exploring the energy spectrum of a four-terminal Josephson junction: Toward topological Andreev band structures, Phys. Rev. X **15**, 031066 (2025).

[44] V. E. Calado, S. Goswami, G. Nanda, M. Diez, A. R. Akhmerov, K. Watanabe, T. Taniguchi, T. M. Klapwijk, and L. M. K. Vandersypen, Ballistic Josephson junctions in edge-contacted graphene, Nat. Nanotechnol. **10**, 761 (2015).

[45] M. Ben Shalom, M. J. Zhu, V. I. Fal'ko, A. Mishchenko, A. V. Kretinin, C. R. Woods, K. Watanabe, T. Taniguchi, A. K. Geim, and J. R. Prance, Quantum oscillations of the critical current and high-field superconducting proximity in ballistic graphene, Nat. Phys. **12**, 318 (2016).

[46] I. V. Borzenets, F. Amet, C. T. Ke, A. W. Draelos, M. T. Wei, A. Seredinski, K. Watanabe, T. Taniguchi, Y. Bomze, M. Yamamoto, S. Tarucha, and G. Finkelstein, Ballistic graphene Josephson junctions from the short to the long junction regimes, Phys. Rev. Lett. **117**, 237002 (2016).

[47] G. Nanda, J. L. Aguilera-Servin, P. Rakyta, A. Kormányos, R. Kleiner, D. Koelle, K. Watanabe, T. Taniguchi, L. M. K. Vandersypen, and S. Goswami, Current-phase relation of ballistic graphene Josephson junctions, Nano Lett. **17**, 3396 (2017).

[48] R. Kraft, J. Mohrmann, R. Du, P. B. Selvasundaram, M. Irfan, U. N. Kanilmaz, F. Wu, D. Beckmann, H. von Löhneysen, R. Krupke, A. Akhmerov, I. Gornyi, and R. Danneau, Tailoring supercurrent confinement in graphene bilayer weak links, Nat. Commun. **9**, 1722 (2018).

[49] M. Zhu, M. Ben Shalom, A. Mishchsenko, V. Fal'ko, K. Novoselov, and A. Geim, Supercurrent and multiple Andreev reflections in micrometer-long ballistic graphene Josephson junctions, Nanoscale **10**, 3020 (2018).

[50] J. Park, J. H. Lee, G.-H. Lee, Y. Takane, K.-I. Imura, T. Taniguchi, K. Watanabe, and H.-J. Lee, Short ballistic Josephson coupling in planar graphene junctions with inhomogeneous carrier doping, Phys. Rev. Lett. **120**, 077701 (2018).

[51] F. E. Schmidt, M. D. Jenkins, K. Watanabe, T. Taniguchi, and G. A. Steele, A ballistic graphene superconducting microwave circuit, Nat. Commun. **9**, 4069 (2018).

[52] P. Pandey, R. Kraft, R. Krupke, D. Beckmann, and R. Danneau, Andreev reflection in ballistic normal metal/graphene/superconductor junctions, Phys. Rev. B **100**, 165416 (2019).

[53] P. Pandey, R. Danneau, and D. Beckmann, Ballistic graphene Cooper pair splitter, Phys. Rev. Lett. **126**, 147701 (2021).

[54] P. Pandey, D. Beckmann, and R. Danneau, Energy distribution controlled ballistic Josephson junction, Phys. Rev. B **106**, 214503 (2022).

[55] P. Schmidt, L. Banszerus, B. Frohn, S. Blien, K. Watanabe, T. Taniguchi, A. K. Hüttel, B. Beschoten, F. Hassler, and C. Stampfer, Tuning the supercurrent distribution in parallel ballistic graphene Josephson junctions, Phys. Rev. Appl. **20**, 054049 (2023).

[56] S. Messelot, N. Aparicio, E. de Seze, E. Eyraud, J. Coraux, K. Watanabe, T. Taniguchi, and J. Renard, Direct measurement of a $\sin(2\varphi)$ current phase relation in a graphene superconducting quantum interference device, Phys. Rev. Lett. **133**, 106001 (2024).

[57] T. Fukui, Y. Hatsugai, and H. Suzuki, Chern numbers in discretized brillouin zone: Efficient method of computing (spin) Hall conductances, J. Phys. Soc. Jpn. **74**, 1674 (2005).

[58] C. W Groth, M. Wimmer, A. R. Akhmerov, and X. Waintal, Kwant: A software package for quantum transport, New J. Phys. **16**, 063065 (2014).

[59] B. van Heck, S. Mi, and A. R. Akhmerov, Single fermion manipulation via superconducting phase differences in multiterminal Josephson junctions, Phys. Rev. B **90**, 155450 (2014).

[60] D. J. Thouless, M. Kohmoto, M. P. Nightingale, and M. den Nijs, Quantized Hall conductance in a two-dimensional periodic potential, Phys. Rev. Lett. **49**, 405 (1982).

[61] All data and simulation codes are available upon reasonable request at (2025), 10.5281/zenodo.14734707